ADVANCED OPTICAL MATERIALS
www.advopticalmat.de

Template Pore Size and A-Site Cation Management Dictate Luminescence Efficiency, Stability, and Wavelength in Confined Perovskite Nanostructures

*Viviana C. P. da Costa, Kyle Frohna, Samuel D. Stranks, and Jeffery L. Coffer**

A-site cation composition is a useful lever in optimizing the photophysical properties and stability of metal halide perovskites (MHPs). Independent of this, straightforward preparative routes to MHP nanostructures that employ a single solid-state template with modest thermal requirements are also in demand. Here both strategies are employed in the fabrication and evaluation of luminescence properties of mixed formamidinium/cesium ($Cs_xFA_{1-x}PbBr_3$) and methylammonium/cesium ($Cs_xMA_{1-x}PbBr_3$) nanostructures formed within confining mesoporous silica of 4 and 7 nm average pore diameters. Use of such small-pore oxide-terminated templates produce perovskite nanostructures in the strongly confined regime, with broadly tunable emission from green to sky blue. It is found that the smallest nanostructures that are formamidinium rich exhibit the largest photoluminescence quantum efficiency values, but such values diminish by more than 50% in a 10 day period. In contrast, the same nanostructures formed within a 7 nm porous template retain their efficiency values over the same time window. The likely origins of this size-dependent behavior are discussed in terms of pore-size-dependent capillary forces. Such routes may ultimately lead to improved light-emitting diode designs composed of controlled quantum-confined perovskites of greater intrinsic stability than other emitters such as ligand-based colloidal nanocrystals.

1. Introduction

The performance of light-emitting diodes (LEDs) composed of metal halide perovskite (MHP) active emitters continues to improve, based on careful refinements in emissive layer composition, structure, and improved carrier injection across injecting interfaces.[1,2] For the first two categories, A-site cation compositional management can be employed to alter the structure and dynamics of metal halide octahedral tilt conformation in the lattice, with consequences for perovskite photophysics and phase stability.[3,4] A recent review emphasizes the important role of thermally activated motion of A-site cations coupled with associated BX_6^{4-} octahedra and their interactions with perovskite charge carriers.[5] Some of the most emissive LEDs and efficient photovoltaics employ perovskite compositions that are in rich in formamidinium (FA)[6] along with a small amount of cesium (Cs);[7–9]strongly emissive LEDs have been achieved using methylammonium (MA)-rich compositions with a small amount of Cs as well.[10]

Complementing the above emphasis on photoluminescence quantum efficiency (PLQE), emission color tunability is also possible in these perovskites based on quantum-confinement effects. Within the quantum-confined regime, three distinct subregimes have been identified for the lead bromide ($PbBr_2$)-based perovskite phases (strong, medium, and weak), with the most sensitive shifts in size-dependent emission maxima falling within the strongly confined regime.[11] The desire to prepare structures emitting in the blue region is especially in demand,[12] as the necessary bandgap in lead halide perovskite films requires bromide–chloride-containing phases that are often unstable; films comprised of quantum dots of this composition are also typically less emissive than their solution analogs.[1,2,9,13–15] Therefore, methods which template the creation of perovskite quantum dots in the smallest size regime, while ideally adding long-term chemical and physical stability to the perovskite,[16,17] are clearly desired.

In this work, we describe the fabrication of a series of lead bromide perovskite nanostructures with mixed formamidinium/cesium ($Cs_xFA_{1-x}PbBr_3$) and methylammonium/cesium ($Cs_xMA_{1-x}PbBr_3$) compositions, with perovskite

V. C. P. da Costa, J. L. Coffer
Department of Chemistry and Biochemistry
Texas Christian University
TCU Box 298860, Fort Worth, TX 76129, USA
E-mail: j.coffer@tcu.edu
K. Frohna, S. D. Stranks
Cavendish Laboratory
University of Cambridge
JJ Thompson Avenue, Cambridge CB3 0HE, UK
S. D. Stranks
Department of Chemical Engineering and Biotechnology
University of Cambridge
Philippa Fawcett Drive, Cambridge CB3 0AS, UK

The ORCID identification number(s) for the author(s) of this article can be found under https://doi.org/10.1002/adom.202202755

DOI: 10.1002/adom.202202755

Table 1. Lead bromide perovskite nanostructures formed within mesoporous silica templates.

Increasing Cs^+ content → for both 4.0 (±0.5) nm and 7.1 (±0.5) nm templates				
$MAPbBr_3$	$MA_{0.90}Cs_{0.10}PbBr_3$	$MA_{0.85}Cs_{0.15}PbBr_3$	$MA_{0.15}Cs_{0.85}PbBr_3$	$CsPbBr_3$
$FAPbBr_3$	$FA_{0.90}Cs_{0.10}PbBr_3$	–	–	

dimension templated by a mesoporous silica (SiO_2) host.[18,19] The goal here is to create new straightforward routes to quantum-confined metal halide perovskites templated by mesoporous solids with the highest possible quantum efficiencies. For these templates, extremely small pore diameters (7 and 4 nm) are necessary to achieve nanostructures in the strong quantum-confined regime. The oxide-terminated host also provides a passivating moiety for surface defects[20–25] and some physical protection against moisture and environmental degradation. Interestingly, it is found that the smallest sub 4 nm nanostructures composed of $Cs_{0.10}FA_{0.90}PbBr_3$ possess extremely strong emission, with PLQE values exceeding 70%. Such values are metastable, however, degrading to 30% within a 10 day period, consistent with the literature for this composition.[7] Significantly, in contrast, the emission for $Cs_{0.10}FA_{0.90}PbBr_3$ created in 7 nm mesoporous silica templates produces a stable structural "sweet spot" with PLQE values being maintained in the 30% range during the same time interval. Analogous methylammonium-containing compositions retain similar trends, albeit with lower absolute emission intensity. The likely origins of this size-dependent behavior are discussed in terms of capillary force-induced out-diffusion of perovskite, along with implications for devices of comparable composition.

2. Results

Previous work from our group and others has established the ability of mesoporous silica,[26,27] mesoporous silicon,[28] and porous silicon nanotubes[29–32] to direct the feature size of nanoscale metal halide perovskites $MAPbX_3$ (X = Br and I), whereby the necessary precursors are carefully infiltrated into a given porous matrix, excess precursor solution removed, and the structure annealed under modest thermal conditions. In this work, we exploit this methodology to create mixed A-site lead bromide compositions using the precursors cesium bromide (CsBr) and formamidinium bromide (FABr) or methylammonium bromide (MABr) in necessary stoichiometric ratios during the above process. In general, precursor solutions of 200 mM concentration are added to milligram quantities of mesoporous SiO_2 powder at slightly elevated temperatures (65–70 °C) to facilitate impregnation, followed by centrifugation, removal of excess supernatant, and heating the resultant powder at 95 °C to crystallize the desired perovskite. The process is visually outlined in Figure S1 (Supporting Information), and the family of structures prepared by this process in this study is listed in **Table 1**.

2.1. Structural Characterization

The resultant products have been structurally characterized by multiple methods, principally transmission electron microscopy (TEM) and powder X-ray diffraction (XRD). **Figure 1** presents TEM images of $Cs_{0.15}MA_{0.85}PbBr_3$ (Figure 1a,b) and $Cs_{0.10}FA_{0.90}PbBr_3$ (Figure 1c,d) formed inside the porous structure of mesoporous silica of 4 and 7 nm average diameters, respectively. For all perovskite compositions, TEM images reveal the presence of spherical perovskite nanostructures with a mean diameter less than the given template pore size. For example, $Cs_{0.10}MA_{0.90}PbBr_3$ nanostructures formed inside a 7 nm template exhibit a mean diameter of 5.7 (±2.2) nm, while the 4 nm pore silica houses 2.7 (±0.7) nm structures. Corresponding values for $Cs_{0.10}FA_{0.90}PbBr_3$ are 4.5 (±1.3) nm and 2.4 (±0.5) nm for the 7 and 4 nm templates, respectively. Associated histograms for these particle sizes are provided in Figure S2 (Supporting Information). Selected nanocrystals typically exhibit lattice spacings associated with the (002) reflection of FA-containing phases[7] or the (200) plane of MA-rich structures[30] (Figure 1d (inset); Figure S2, Supporting Information).

Powder X-ray diffraction measurements provide necessary phase information for these structures along with a Halder–Wagner-type analysis[33] of XRD line shape, providing particle size information for selected nanostructures. **Figure 2** shows the evolution of diffraction patterns with A-site composition. The observed pattern for $CsPbBr_3$ is consistent with the established orthorhombic phase (space group *Pnma*),[34,35] while for $FAPbBr_3$ and $MAPbBr_3$ the proper description is cubic ($Pm\bar{3}m$).[34,36–38] The Cs-rich composition $Cs_{0.85}MA_{0.15}PbBr_3$ shows an orthorhombic-like phase pattern with regard to the number of peaks, associated 2θ values and their relative intensities.

Analysis of the X-ray data using the Halder–Wagner model provides a complementary assessment of average particle size for selected perovskites. For the example of perovskite nanostructures confined within a 7 nm mesopore, an average value of 8.0 (±1.5) nm is extracted for $Cs_{0.85}MA_{0.15}PbBr_3$, while $Cs_{0.10}MA_{0.90}PbBr_3$ yields 6.0 (±1.9) nm, both in reasonable agreement with corresponding TEM analyses (within a nanometer or less). Similar examples are found for perovskite nanostructures formed within 4 nm pores; for $MAPbBr_3$ and $FAPbBr_3$, average particle sizes of 2.8 (±0.4) and 3.6 (±0.7) nm, respectively, are found. Representative Halder–Wagner plots for the above are provided in Figure S3 (Supporting Information).

2.2. Photoluminescence Properties

We begin this section with the question of size control and associated emission wavelength of a given perovskite. We vary both the composition of the A-site of the perovskite as well as the lower limit of mesoporous silica pore diameter to 4 nm, thereby significantly shifting the associated emission maximum into the sky blue region (CIE-*X*: 0.0234, *Y*: 0.413).

This effect is exemplified by a comparison of emission maxima for the homogeneous A-site compositions $FAPbBr_3$, $MAPbBr_3$, and $CsPbBr_3$ formed within 4 and 7 nm pore diameter mesoporous silica, along with a bulk reference sample (**Table 2**; Figure S3, Supporting Information). Here the overall blueshift in PL maximum from bulk to the smallest nanostructure formed (within the 4 nm mesoporous template) is ≈193 meV for $FAPbBr_3$, ≈198 meV for $MAPbBr_3$, and ≈148 meV for

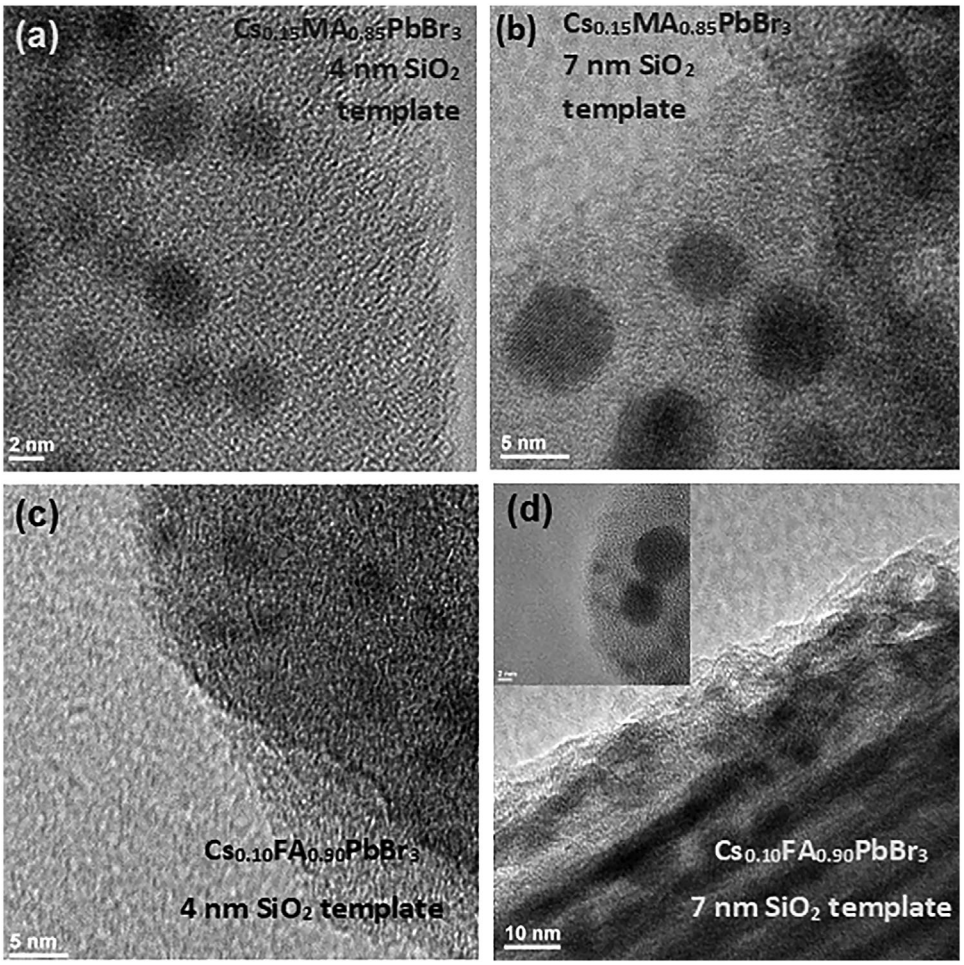

Figure 1. TEM images of $Cs_{0.15}MA_{0.85}PbBr_3$ in a) 4 nm and b) 7 nm pore diameter templates and $Cs_{0.10}FA_{0.90}PbBr_3$ in c) 4 nm and d) 7 nm pore templates.

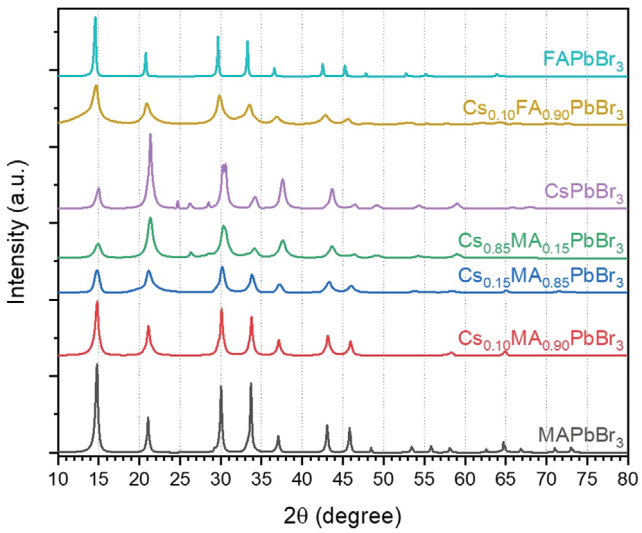

Figure 2. X-ray diffraction spectra for the series of $Cs_xFA_{1-x}PbBr_3$ and $Cs_xMA_{1-x}PbBr_3$ nanostructures formed within mesoporous silica with a 7 nm pore diameter.

Table 2. Emission maxima wavelength (nm) for $FAPbB_{r3}$, $MAPbBr_3$, and $CsPbBr_3$ as a function of perovskite crystal size (λ_{ex} = 370 nm).

Perovskite composition	4 nm	7 nm	Bulk
$FAPbB_{r3}$	499 ± 1.4	529 ± 2.5	541 ± 0.6
$MAPbBr_3$	495 ± 0.7	519 ± 1.2	538 ± 2.2
$CsPbBr_3$	494 ± 0.5	513 ± 0.7	525 ± 1.4

$CsPbBr_3$. The mixed A-site compositions thus follow a similar trend, exemplified by the PL spectra of $Cs_{0.10}MA_{0.90}PbBr_3$ and $Cs_{0.10}FA_{0.90}PbBr_3$ shown as a function of size in **Figure 3**.

It should be noted that for a given template size, the emission maximum is only subtly affected by A-site ratios of Cs to MA or Cs to FA in the corresponding perovskite; the range of PL max for structures formed within the 4 nm template is ≈28 meV, while for the 7 nm template it is somewhat larger at ≈69 meV (Figure S4, Supporting Information).

The most significant influence of A-site composition is manifested in the PLQE (**Figure 4**), evaluated under a steady-state excitation density of 18 mW cm^{-2} at 405 nm. Three important trends

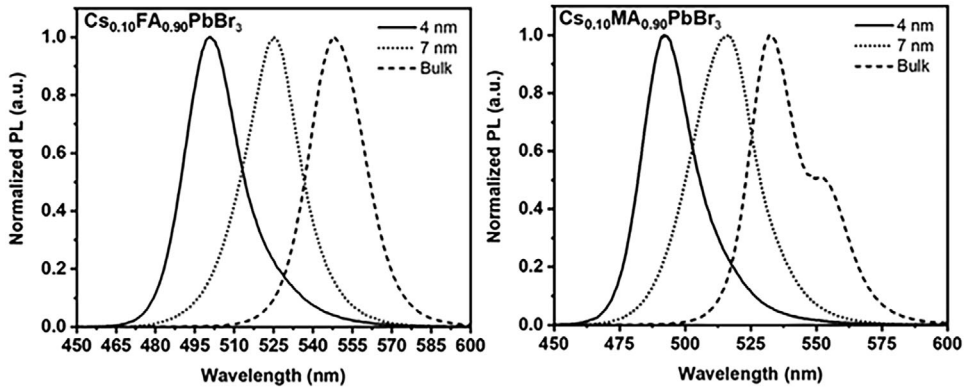

Figure 3. Room-temperature PL spectra for $Cs_{0.10}FA_{0.90}PbBr_3$ and $Cs_{0.10}MA_{0.90}PbBr_3$ as a function of template size (4 vs 7 nm vs bulk). The presence of the lower energy peak in the $Cs_{0.10}MA_{0.90}PbBr_3$ bulk sample, as well as in bulk $CsPbBr_3$ and $MAPbBr_3$ (Figure S3, Supporting Information), infers some degree of phase heterogeneity in the nontemplated samples.

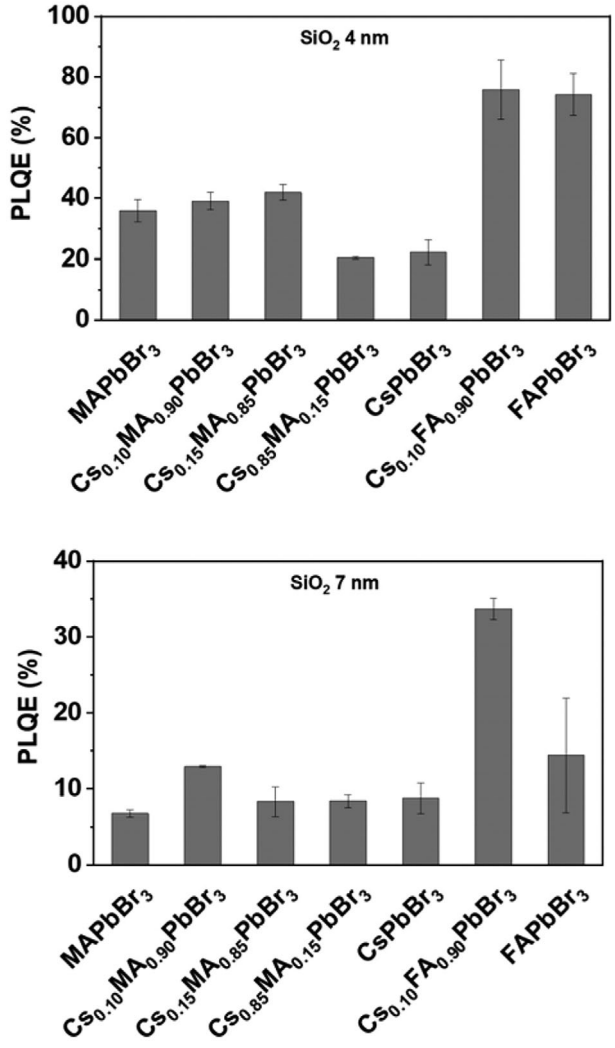

Figure 4. PLQE values for selected nanoscale $Cs_xFA_{1-x}PbBr_3/Cs_xMA_{1-x}PbBr_3$ perovskites formed within 4 and 7 nm pore mesoporous silica templates. All samples were exposed to vacuum immediately before measurement and otherwise stored in a desiccator.

are observed. First, for those perovskites with comparable composition, structures formed within the 4 nm template demonstrate PLQE values more than twice than those housed within the 7 nm pore silica (at a minimum); for example, $Cs_{0.10}FA_{0.90}PbBr_3$ formed within the 4 nm pore template exhibits a PLQE value of 76%, while the same composition structure formed within the 7 nm porous template is ≈34%. Second, for perovskites of comparable A-site ratio of organo-ammonium:cesium and template pore size, swapping methylammonium for formamidinium with results in a significantly larger PLQE for the FA-containing species (e.g., PLQE of $Cs_xFA_{1-x}PbBr_3 \gg Cs_xMA_{1-x}PbBr_3$). For example, $Cs_{0.10}FA_{0.90}PbBr_3$ formed within the 7 nm template possesses a PLQE value of 34%, while $Cs_{0.10}MA_{0.90}PbBr_3$ also formed within this same mesoporous silica with 7 nm pores yields a substantially less emissive perovskite with a PLQE of ≈13%.

Investigations of fluence dependence on these samples in the 18–630 mW cm^{-2} range reveal highest PLQE values at lower fluences, then dropping off slightly before leveling off (for example, 30% vs 25% for $Cs_{0.10}FA_{0.90}PbBr_3$; Figure S6, Supporting Information). Thus, even at such low fluences, it appears that the traps are saturated; similar trends have been observed for nanocrystals whereby PL intensity as a function of carrier concentration presents a linear or slightly sublinear response, suggesting the PLQE is essentially constant.[39]

For the $Cs_xMA_{1-x}PbBr_3$ series, incorporation of excess Cs ($x > 0.2$) results in a marked reduction in PLQE, as evidenced in the 4 nm pore template results. At $x = 0.10$ or 0.15, PLQE values of ≈40% are obtained, while at the other extreme $x = 0.85$ the value drops to roughly half, ≈20%. Such a reduction is likely associated with increased energy transfer to trap states and rougher surface morphology (with defects).[7] Third, and significantly, it must be emphasized that the PLQE values for $Cs_{0.10}MA_{0.90}PbBr_3$ and $Cs_{0.10}FA_{0.90}PbBr_3$ formed within a 4 nm mesoporous silica template are metastable. For example, for samples exposed to vacuum immediately before measurement (and otherwise stored in a desiccator), the ≈76% PLQE value for $Cs_{0.10}FA_{0.90}PbBr_3$ formed within 4 nm mesoporous silica degrades somewhat to 28%—still a significant value—within a 10 day period, consistent with the behavior of octylamine/oleic acid-stabilized 10 nm FA-rich lead bromide perovskite nanocrystals (including those with

Table 3. Changes in PLQE values for selected perovskites as a function of sample ageing.

Perovskite composition	Template (SiO_2) pore diameter [nm]	PLQE [%]	
		Fresh sample	10 days Aged sample
$Cs_{0.10}FA_{0.90}PbBr_3$	4	75.8	27.9
	7	33.7	29.7
$Cs_{0.10}MA_{0.90}PbBr_3$	4	39.1	15.2
	7	12.9	14.8

this composition) observed previously in the literature.[7] This known limited stability (36 h) of PLQE values for selected ligand-stabilized formamidinium-rich lead bromide perovskite nanostructures was a significant consideration in our selecting a 10 day observation window for tracking the stability of these new templated perovskite nanostructures.

Such a behavior is not restricted to FA-containing compositions. Small nanocrystals of $Cs_{0.10}MA_{0.90}PbBr_3$ formed within the 4 nm templates behave similarly, diminishing from an initial value of 39% to 15% at the same time interval (**Table 3**).

Significantly, in contrast to the above loss of PLQE for the above 4 nm perovskite nanostructures, the perovskite emission created in 7 nm mesoporous silica templates produces relatively stable PLQE values remaining essentially unchanged during the same time interval. In particular, the PLQE value of $Cs_{0.10}MA_{0.90}PbBr_3$ remains in the 15% range after ≈10 days ageing, and while that of $Cs_{0.10}FA_{0.90}PbBr_3$ stays ≈30% (Table 3).

3. Discussion

Nanoporous template infiltration of precursor solutions composed of proper stoichiometric ratios of MABr (or FABr), CsBr, and $PbBr_2$ in *N*,*N*-dimethylformamide (DMF), followed by a modest thermal anneal (90 °C for ≈60 min), is a straightforward way to create dispersed nanocrystals of metal halide perovskites of mixed A-site cations such as $Cs_{0.10}MA_{0.90}PbBr_3$ and $Cs_{0.10}FA_{0.90}PbBr_3$. Mesoporous silica is an ideal template for this purpose, as it provides oxide moieties that can passivate defects of the perovskite, and importantly, is available in ultrasmall pore diameters that can restrict the dimensions of the resultant perovskite well into the quantum-confined regime.

Discussion of perovskite photophysics mandates the need for clear phase identification. Powder XRD diffraction provides such detail. Cs-rich structures exhibit an orthorhombic-type unit cell, with FA- and MA-based compositions possessing a cubic lattice. The incorporation of small amounts of Cs into lead halide perovskite compositions is firmly established to bring marked phase stability to the structure.[40] It is also likely that the excess surface energy brought about by the reduced size of the nanocrystals plays a role in stabilizing a given phase.[41]

The sizes of perovskite nanostructures generated by use of these mesoporous silica templates fall clearly into the strongly confined region, producing bright sky blue emission (CIE-*X*: 0.0234,*Y*: 0.413) for the smallest nanostructures formed within the 4 nm templates, in contrast to the limited blueshifts in the emission maxima of the perovskite when mesoporous templates in the 7–18 nm pore range are used and emission remains in the green range.[26]

For the single identity A-site perovskites (i.e., $FAPbBr_3$, $MAPbBr_3$, and $CsPbBr_3$) it is clear that the emission maximum of the Cs derivative is the most blueshifted for a given size, consistent with the greatest tilt angle of the [$PbBr_6^{4-}$] octahedra. Recent computational studies by Mannino et al. indicate that while the bandgap of an $XPbBr_3$ sample can increase by either an isotropic volume expansion or by the tilting of [$PbBr_6^{4-}$], octahedral tilting takes a primary role in shaping the bandgap value for these three perovskites.[34]

Likely the most noteworthy point of interest in these measurements lies with respect to PLQE values as a function of A-site composition and template pore diameter. The fact that the $Cs_{0.10}FA_{0.90}PbBr_3$ system is the most emissive of the compositions evaluated here is consistent with previous work by Zhang et al., which noted, for the series of $Cs_xFA_{1-x}PbBr_3$ (x = 0–0.6), that the $x = 0.1$ possesses the largest PLQE, with an initial value of 73%.[7] Cs-rich $FAPbBr_3$ nanocrystal(NC) emitter-based LEDs have also been reported to possess PLQE values above 60%.[9] This enhanced PL in both our templated perovskite nanocrystals and the ligand-passivated lead bromide NCs reported earlier is most readily explained by confined systems exhibiting increased radiative rates, but contributions from increased radiative lifetime to the observed steady-state PL intensity through defect reduction are also possible.[7] Such FA-rich systems lack long-term stability with regard to PL intensity,; however.[7] The PLQE of the NC composition reported by Zhang et al. degrades to 41% within 36 h. This specific degradation is associated with carrying out the above measurements in moist air and subsequent formation of perovskite degradation products.

In our structures, the time-based evolution of the PL of the metastable $Cs_{0.10}FA_{0.90}PbBr_3$ compositions formed within the 4 nm mesopores is consistent with out diffusion of the perovskite from the pores (**Figure 5**) and onto the outer surface of silica. For samples exposed to vacuum immediately before measurement (and otherwise stored in a desiccator), a longer wavelength shoulder appears in the PL spectrum over time, consistent with the out diffusion of the perovskite nanostructures from the silica pore, or selective diffusion of Cs-rich material from the porous matrix. This evolution of the emission spectrum of the perovskite embedded in a porous matrix from pore-confined to free film has been observed previously in the case of $MAPbI_3$ located in a porous silicon matrix, the driving force for the process in this case being the hydrophobic porous Si surface.[26] Careful analysis of selected samples in this category by high-resolution TEM (HRTEM) does show some perovskite material outside of the pore and is

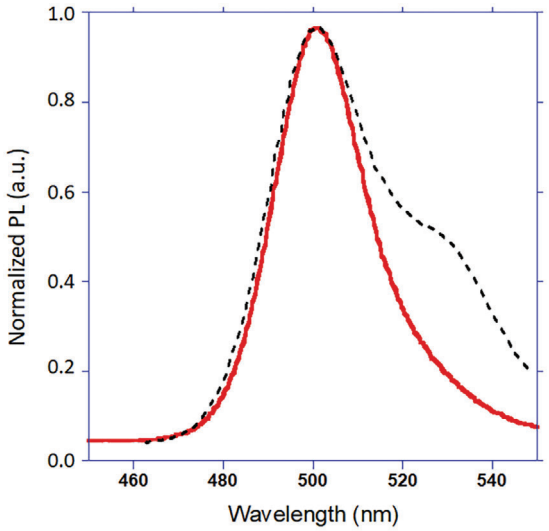

Figure 5. PL spectra of freshly prepared $Cs_{0.10}FA_{0.90}PbBr_3$ (solid black line) and stored under vacuum for 10 days (dashed black line).

consistent with this conclusion, but it cannot be excluded with absolute certainty that the specific isolated nanosized feature observed was not originally formed outside of the pore.

In contrast, the PLQE for perovskites formed within the slightly larger 7 nm mesopores does not change significantly during the same period. This is likely a consequence of a relative "sweet spot" of stability in the 7 nm pore. Given the inverse relationship between capillary pressure exerted by a given nanopore and pore diameter,[42] the capillary force exerted on a loaded perovskite nanocrystal is roughly 50% higher for the smaller 4 nm nanopore than the 7 nm analog. The application of extended vacuum likely induces movement of the perovskite and its subsequent environmental degradation. Such an effect is strongly dependent on the initial relative location of the perovskite nanostructure within the porous framework.

For the 7 nm pore template, the phase stabilization influence of Cs incorporation into the FA and MA framework is also more evident in the PLQE values when the A-site Cs content is at 10 at%. It is anticipated that the incorporation of Cs into a given perovskite alters the degree of lead bromide octahedral tilt, as the XRD pattern for $Cs_xFA_{1-x}PbBr_3$ more closely resembles a cubic (rather than orthorhombic) phase and thus the volume contraction with Cs incorporation to be of lesser importance here.[34]

4. Conclusion

The results shown here illustrate the ability to create highly emissive perovskite nanostructures through a straightforward preparative route with size directed by passivating mesoporous silica templates. Similar to technologically relevant thin films, the optimal luminescence efficiency in these nanostructures is generated in mixtures of cesium and formamidinium at the A-site. The challenges associated with fabricating ultrasmall (<8 nm) perovskite nanocrystals in such pores are evident. The semiconductor nanostructure must be housed relatively deep within the pores to avoid desorption and ultimately degradation, challenging for 4 nm pores, easier for 7 nm ones. Carrying out detailed time-resolved measurements in the near term may assist in answering fundamental questions of these mixed A-cation perovskites regarding similar PLQE of the aged samples (despite the different pore sizes). Packaging such structures into functional LED platforms may provide some additional stability, and such experiments are planned for the near future. Other device platforms are possible with this configuration (e.g., scintillators and detectors) and warrant serious consideration. However, fundamentally a need also exists for the assessment of the properties of the quantum dots away from these mesoporous templates, and this remains a future goal.

5. Experimental Section

Materials: Lead bromide (≥98%), methylammonium bromide (98%), formamidinium bromide (≥99%, anhydrous), cesium bromide (99.99%), DMF (≥99.7%), dimethyl sulfoxide (DMSO, ≥99.5% anhydrous), and mesoporous silica powder ($d_{pore} \approx 7.1$ nm, $d_{pore} \approx 4$ nm) were purchased from Sigma–Aldrich. All of the above chemicals were used without further purification.

Preparation of Perovskite Precursor Solutions: Lead bromide perovskites of pure cations, $APbBr_3$ with A = MA^+, FA^+, or Cs^+, were prepared by mixing, at room temperature, equimolar amounts (200 mM) of DMF or DMSO solutions of ABr + $PbBr_2$. More complex perovskite precursor solutions, with mixed cations, were also prepared, namely $Cs_{0.10}MA_{0.80}PbBr_3$, $Cs_{0.15}MA_{0.85}PbBr_3$, $Cs_{0.85}MA_{0.15}PbBr_3$, and $Cs_{0.10}FA_{0.90}PbBr_3$. These complex solutions were prepared using the same procedure as above but with different molar concentrations. For instance, $Cs_{0.15}MA_{0.85}PbBr_3$ was prepared using DMSO solutions of 30 mM CsBr + 30 mM MABr + 200 mM $PbBr_2$. All solutions were sonicated for 5–10 min, followed by vortex stirring, to ensure complete dissolution and mixing. The prepared transparent solution was used as was for the preparation of the silicon-perovskite-based materials as well as bulk perovskite structures.

Preparation of Perovskite Bulk Structures: Perovskite bulk structures were prepared by placing ≈0.1 mL of perovskite precursor solution on a piece of fluorine-doped tin oxide (FTO) glass. The sample on the FTO glass was then heated for 30 min at 95 °C. Characterization was performed on freshly prepared samples and aged samples kept in a desiccator.

Preparation of Silicon Perovskite-Containing Materials: In a given experiment, 1 mL of perovskite precursor solution at 200 mM Pb^{2+} concentration was added to 10 mg of mesoporous SiO_2 powder. This mixture was then heated at 65–70 °C under stirring for 4 h for complete impregnation of the precursor solution within the SiO_2 mesoporous structure. Afterward, the mixture was centrifuged for ≈3 min. The supernatant liquid was removed using a micropipette, and the remaining SiO_2 powder was collected using a spatula. The as-obtained powder was then sandwiched between two microscope glass plates and heated at 95 °C for 40 min. The resulting perovskite-impregnated powder was then placed under vacuum for 2 days for complete solvent removal. The freshly obtained materials were then characterized. After initial characterization, the prepared materials were stored and aged in a desiccator and used for further analyses. For PLQE measurements specifically, the ability of mesoporous solids to rapidly adsorb atmospheric species, and the established passivating role of oxygen for perovskite PL intensity, led to store these samples under a modest vacuum (10^{-3} Torr) where ample oxygen was still present, but moisture was relatively excluded. This treatment was confirmed empirically to yield the highest intensity PL spectra.

Material Characterization: TEM images were obtained using a JEOL JEM-2100, operating at an acceleration potential of 200 kV. Field emission scanning electron microscopy (FE-SEM) was also used for complimentary imaging through the use of a JEOL-JSM-7100F. Powder XRD data were collected using a Rigaku SmartLab SE with a HyPix detector using Cu Kα radiation with a step size of 0.01° and a scan speed of 0.80° min^{-1} in the 10°–80° 2θ range. Steady-state PL spectroscopy was measured on samples mounted with carbon tape using a Nikon Optiphot Fluorescence

microscope with an Hg lamp and excitation filter centered at 370 nm and interfaced to an Ocean Optics spectrometer. PLQE was measured according to published procedures[43] using an integrated sphere from Newport using a laser excitation wavelength of 405 nm at a steady-state excitation density of 18 mW cm^{-2}. For a given sample, PLQE was measured in air after samples were exposed to a modest (10^{-2} Torr) vacuum overnight to minimize the impact of oxygen in these measurements; samples were kept in a desiccator when not being evaluated.

Supporting Information

Supporting Information is available from the Wiley Online Library or from the author.

Acknowledgements

The authors gratefully thank the Robert A. Welch Foundation for financial support (Grant P-1212, J.L.C.). K.F. acknowledges a George and Lilian Schiff Studentship, Winton Studentship, the Engineering and Physical Sciences Research Council (EPSRC) studentship, Cambridge Trust Scholarship, and Robert Gardiner Scholarship. S.D.S. acknowledges the Royal Society and Tata Group (Grant no. UF150033). The work received funding from the European Research Council under the European Union's Horizon 2020 research and innovation programme (HYPERION, Grant agreement No. 756962). The authors acknowledge the EPSRC (Grant No. EP/R023980/1) for funding.

Conflict of Interest

The authors declare no conflict of interest.

Author Contributions

V.C.P.d.C. and J.L.C. designed most of the experiments. V.C.P.d.C. carried out the preparation and characterization of the perovskite/mesoporous template materials. K.F. carried out PLQE measurements on aged samples. V.C.P.d.C., J.L.C., K.F., and S.D.S. all contributed to writing and editing of the manuscript.

Data Availability Statement

The data that support the findings of this study are available from the corresponding author upon reasonable request.

Keywords

confined perovskites, mesoporous silica, photoluminescence, quantum confinement, stability

Received: November 18, 2022
Revised: May 2, 2023
Published online: June 1, 2023

[1] X.-K. Liu, W. Xu, S. Bai, Y. Jin, J. Wang, R. H. Friend, F. Gao, *Nat. Mater.* **2021**, *20*, 10.
[2] K. Ji, M. Anaya, A. Abfalterer, S. D. Stranks, *Adv. Opt. Mater.* **2021**, *9*, 2002128.
[3] T. A. S. Doherty, S. Nagane, D. J. Kubicki, Y.-K. Jung, D. N. Johnstone, A. N. Iqbal, D. Guo, K. Frohna, M. Danaie, E. M. Tennyson, S. Macpherson, A. Abfalterer, M. Anaya, Y.-H. Chiang, P. Crout, F. S. Ruggeri, S. Collins, C. P. Grey, A. Walsh, P. A. Midgley, S. D. Stranks, *Science* **2021**, *374*, 1598.
[4] F. Ünlü, E. Jung, J. Haddad, A. Kulkarni, S. Öz, H. Choi, T. Fischer, S. Chakraborty, T. Kirchartz, S. Mathur, *APL Mater.* **2020**, *8*, 070901.
[5] J.-W. Lee, S. Tan, S. I. Seok, Y. Yang, N.-G. Park, *Science 375*, eabj1186.
[6] C. Qin, T. Matsushima, W. J. Potscavage, A. S. D. Sandanayaka, M. R. Leyden, F. Bencheikh, K. Goushi, F. Mathevet, B. Heinrich, G. Yumoto, Y. Kanemitsu, C. Adachi, *Nat. Photonics* **2020**, *14*, 70.
[7] X. Zhang, H. Liu, W. Wang, J. Zhang, B. Xu, K. L. Karen, Y. Zheng, S. Liu, S. Chen, K. Wang, X. W. Sun, *Adv. Mater.* **2017**, *29*, 1606405.
[8] B. G. H. M. Groeneveld, S. Adjokatse, O. Nazarenko, H.-H. Fang, G. R. Blake, G. Portale, H. Duim, G. H. ten Brink, M. V. Kovalenko, M. A. Loi, *Energy Technol.* **2020**, *8*, 1901041.
[9] Y. Liu, J. Cui, K. Du, H. Tian, Z. He, Q. Zhou, Z. Yang, Y. Deng, D. Chen, X. Zuo, Y. Ren, L. Wang, H. Zhu, B. Zhao, D. Di, J. Wang, R. Friend, Y. Jin, *Nat. Photonics* **2019**, *13*, 760.
[10] L. Zhang, X. Yang, Q. Jiang, P. Wang, Z. Yin, X. Zhang, H. Tan, Y. Yang, M. Wei, B. R. Sutherland, E. H. Sargent, J. You, *Nat. Commun.* **2017**, *8*, 15640.
[11] M. A. Becker, R. Vaxenburg, G. Nedelcu, P. C. Sercel, A. Shabaev, M. J. Mehl, J. G. Michopoulos, S. G. Lambrakos, N. Bernstein, J. L. Lyons, T. Stöferle, R. F. Mahrt, M. V. Kovalenko, D. J. Norris, G. Rainò, A. L. Efros, *Nature* **2018**, *553*, 189.
[12] V. Malgras, J. Henzie, T. Takei, Y. Yamauchi, *Angew. Chem., Int. Ed.* **2018**, *57*, 8881.
[13] M. K. Gangishetty, S. Hou, Q. Quan, D. Congreve, *Adv. Mater.* **2018**, *30*, 1706226.
[14] Y. Jiang, C.-c. Qin, M. Cui, T. He, K. Liu, Y. Huang, M. Luo, L. Zhang, H. Xu, S. Li, J. Wei, Z. Liu, H.-h. Wang, G.-H. Kim, M. Yuan, J. Chen, *Nat. Commun.* **2019**, *10*, 1868.
[15] Y. Fu, S. Poddar, B. Ren, Y. Xie, Q. Zhang, D. Zhang, B. Cao, Y. Tang, Y. Ding, X. Qiu, L. Shu, J.-F. Liao, D.-B. Kuang, Z. Fan, *ACS Nano* **2022**, *16*, 8388.
[16] G. Mannino, I. Deretzis, E. Smecca, F. Giannazzo, S. Valastro, G. Fisicaro, A. La Magna, D. Ceratti, A. Alberti, *J. Phys. Chem. C* **2021**, *125*, 4938.
[17] A. García-Fernández, E. J. Juarez-Perez, S. Castro-García, M. Sánchez-Andújar, L. K. Ono, Y. Jiang, Y. Qi, *Small Methods* **2018**, *2*, 1800242.
[18] V. Malgras, S. Tominaka, J. W. Ryan, J. Henzie, T. Takei, K. Ohara, Y. Yamauchi, *J. Am. Chem. Soc.* **2016**, *138*, 13874.
[19] A. Rubino, L. Caliò, A. García-Bennett, M. E. Calvo, H. Míguez, *Adv. Opt. Mater.* **2020**, *8*, 1901868.
[20] H. Dong, C. Zhang, W. Nie, S. Duan, C. N. Saggau, M. Tang, M. Zhu, Y. S. Zhao, L. Ma, O. G. Schmidt, *Angew. Chem., Int. Ed.* **2022**, *61*, e202115875.
[21] R. Brenes, D. Guo, A. Osherov, N. K. Noel, C. Eames, E. M. Hutter, S. K. Pathak, F. Niroui, R. H. Friend, M. S. Islam, H. J. Snaith, V. Bulović, T. J. Savenije, S. D. Stranks, *Joule* **2017**, *1*, 155.
[22] M. Anaya, J. F. Galisteo-López, M. E. Calvo, J. P. Espinós, H. Míguez, *J. Phys. Chem. Lett.* **2018**, *9*, 3891.
[23] R. Brenes, C. Eames, V. Bulović, M. S. Islam, S. D. Stranks, *Adv. Mater.* **2018**, *30*, 1706208.
[24] Y. Tian, M. Peter, E. Unger, M. Abdellah, K. Zheng, T. Pullerits, A. Yartsev, V. Sundström, I. G. Scheblykin, *Phys. Chem. Chem. Phys.* **2015**, *17*, 24978.
[25] D. Lu, Y. Zhang, M. Lai, A. Lee, C. Xie, J. Lin, T. Lei, Z. Lin, C. S. Kley, J. Huang, E. Rabani, P. Yang, *Nano Lett.* **2018**, *18*, 6967.
[26] V. C. P. da Costa, R. Gonzalez-Rodriguez, K. Frohna, G. Delport, S. D. Stranks, L. T. Canham, J. L. Coffer, *Adv. Mater. Interfaces* **2020**, *7*, 2001138.

[27] D. N. Dirin, L. Protesescu, D. Trummer, I. V. Kochetygov, S. Yakunin, F. Krumeich, N. P. Stadie, M. V. Kovalenko, *Nano Lett.* **2016**, *16*, 5866.
[28] S. Demchyshyn, J. M. Roemer, H. Groiß, H. Heilbrunner, C. Ulbricht, D. Apaydin, A. Böhm, U. Rütt, F. Bertram, G. Hesser, M. C. Scharber, N. S. Sariciftci, B. Nickel, S. Bauer, E. D. Głowacki, M. Kaltenbrunner, *Sci. Adv.* **2017**, *3*, e1700738.
[29] R. Gonzalez-Rodriguez, N. Arad-Vosk, A. Sa'ar, J. L. Coffer, *J. Phys. Chem. C* **2018**, *122*, 20040.
[30] R. Gonzalez-Rodriguez, V. C. P. Costa, G. Delport, K. Frohna, R. L. Z. Hoye, S. D. Stranks, J. L. Coffer, *Nanoscale* **2020**, *12*, 4498.
[31] R. Gonzalez-Rodriguez, N. Arad-Vosk, N. Rozenfeld, A. Sa'ar, J. L. Coffer, *Small* **2016**, *12*, 4477.
[32] N. Arad-Vosk, N. Rozenfeld, R. Gonzalez-Rodriguez, J. L. Coffer, A. Sa'ar, *Phys. Rev. B* **2017**, *95*, 085433.
[33] D. Nath, F. Singh, R. Das, *Mater. Chem. Phys.* **2020**, *239*, 122021.
[34] G. Mannino, I. Deretzis, E. Smecca, A. La Magna, A. Alberti, D. Ceratti, D. Cahen, *J. Phys. Chem. Lett.* **2020**, *11*, 2490.
[35] S. Hirotsu, J. Harada, M. Iizumi, K. Gesi, *J. Phys. Soc. Jpn.* **1974**, *37*, 1393.
[36] M. Keshavarz, M. Ottesen, S. Wiedmann, M. Wharmby, R. Küchler, H. Yuan, E. Debroye, J. A. Steele, J. Martens, N. E. Hussey, M. Bremholm, M. B. J. Roeffaers, J. Hofkens, *Adv. Mater.* **2019**, *31*, 1900521.
[37] E. C. Schueller, G. Laurita, D. H. Fabini, C. C. Stoumpos, M. G. Kanatzidis, R. Seshadri, *Inorg. Chem.* **2018**, *57*, 695.
[38] C. Abia, C. A. López, M. C. Álvarez-Galván, L. Canadillas-Delgado, M. T. Fernández-Díaz, J. A. Alonso, *J. Mater. Chem. C* **2021**, *9*, 17003.
[39] S. Feldmann, M. K. Gangishetty, I. Bravić, T. Neumann, B. Peng, T. Winkler, R. H. Friend, B. Monserrat, D. N. Congreve, F. Deschler, *J. Am. Chem. Soc.* **2021**, *143*, 8647.
[40] E. M. Mozur, M. A. Hope, J. C. Trowbridge, D. M. Halat, L. L. Daemen, A. E. Maughan, T. R. Prisk, C. P. Grey, J. R. Neilson, *Chem. Mater.* **2020**, *32*, 6266.
[41] X. Kong, K. Zong, S. S. Lee, *Chem. Mater.* **2019**, *31*, 4953.
[42] H. J. Butt, K. Graf, M. Kappl, *Physics and Chemistry of Interfaces*, 3rd ed., Wiley VCH, Weinheim **2013**.
[43] S. Leyre, E. Coutino-Gonzalez, J. J. Joos, J. Ryckaert, Y. Meuret, D. Poelman, P. F. Smet, G. Durinck, J. Hofkens, G. Deconinck, P. Hanselaer, *Rev. Sci. Instrum.* **2014**, *85*, 123115.